NIPPON STEEL TECHNICAL REPORT No. 136 JULY 2026

Technical Report

Numerical Simulation Model of Gas-Liquid-Solid Flows with Gas-Liquid Free Surface and Solid Particles Flows

Kengo KIHARA* Nobuhiro OKADA

Abstract

Gas-liquid-solid flow is an important phenomenon in large-scale industrial processes. The difficulties in numerical simulations of these processes lie in the problems of the high calculation cost for a large-scale system, the simultaneous occurrence of dispersed and sedimented particle flows, and the coexistence of solid particles and a gas-liquid free surface. In this study, a numerical simulation model of gas-liquid-solid flows was developed based on the continuum description. The volume-of-fluid (VOF) method and granular flow model were coupled in the proposed model. As a result, the proposed model is applicable to gas-liquid-solid flows where a gas-liquid free surface and solid-particle flows coexist. In addition, the use of the granular flow model enabled simultaneous simulations of dispersed and sedimented particle flows. Based on the continuum description, the proposed model has the advantage of low calculation cost compared to the DEM-VOF method. To verify the model, the results of the numerical simulations were compared with the simulation results using the DEM-VOF method, experimental results, or theoretical relationships. These comparisons indicate that the proposed model is reasonably applicable to the gas-liquid-solid flows.

1. Introduction

Fluid-solid particle mixtures frequently occur in industrial processes. Numerical calculation techniques for predicting particle motion in fluids have long been developed and applied to various industrial processes. For example, the discrete phase model (DPM) and multi-fluid models based on continuum descriptions are widely used for the motion of dilute dispersed particles,[1, 2] while models based on kinetic theory and the discrete element method (DEM) are commonly employed for systems involving intense particle collisions.[3, 4] The latter DEM is also frequently used for calculating flows of solid particle deposits.[5] However, these numerical calculations often target only one phase—either the gas or liquid phase—as the fluid phase. Reports on numerical calculations for solid-gas-liquid three-phase flows involving gas-liquid free interfaces are scarce. Such calculations require coupling with free-surface calculation methods, such as the volume-of-fluid (VOF) method[6] or the level set method[7].

DEM can be relatively easily applied to numerical calculations considering both dispersed and deposited particles. Sun and Sakai[8] proposed the DEM-VOF method for numerical calculations of solid-gas-liquid three-phase flows. They used this method to simulate the water entry behavior of solid particles and dam break simulations involving sediment particles. However, numerical calculations using DEM face high computational costs as the number of solid particles increases, making it challenging to apply them to large-scale industrial processes, both spatially and temporally.

Multi-fluid models based on continuum descriptions are highly effective for large-scale system simulations because computational cost is not directly influenced by particle count. Models based on kinetic theory are suitable for accounting for collisions between solid particles.[9] These models have long been used to calculate solid particle flow in fluidized beds of solid-gas and solid-liquid systems,[10, 11] but generally do not consider rheology within packed beds. On the other hand, several numerical calculation models for flow in packed particle layers using continuum descriptions have also been proposed.[12, 13] These models incorporate the rheology of packed parti-

* Researcher, Mathematical Science & Technology Research Lab., Advanced Technology Research Laboratories
20-1 Shintomi, Futtsu City, Chiba Pref. 293-8511

cle layers using methods such as the Coulomb model or μ-(I) rheology[14], but they assume incompressibility for particle flow and do not account for particle dispersion.

Lee et al.[15] proposed a numerical calculation model considering dispersion and the flow of packed particulate matter. This model is based on kinetic theory and model equations concerning enduring-contact within the packed particulate matter.[16, 17] In this model, the stress tensor is decomposed into kinetic and enduring-contact components. The kinetic stress tensor employs kinetic theory, while the shear stress due to enduring-contact uses the Coulomb model. Furthermore, since this model is based on a continuum description, it is expected to be applicable to large-scale industrial processes at low computational cost. To apply this model to solid-gas-liquid three-phase flows involving free surfaces, coupling techniques with methods such as the VOF method are required.

In this study, a numerical calculation model for solid-gas-liquid three-phase flow was constructed using the VOF method and the powder particle model reported by Lee et al.[15]. The proposed model is applicable to systems where free surfaces and solid particle flows coexist. To verify the model's accuracy, numerical calculations were performed for three systems and compared with DEM-VOF method calculations, experiments, and theoretical equations. The first system involved granular collapse of heavy solid particles below the gas-liquid interface,[18] the second system involved granular collapse of light solid particles at the gas-liquid interface,[19] and the third system concerned the floatation and oscillation of a group of light solid particles at the gas-liquid interface.

2. Numerical Analysis Model

2.1 Governing equations

This model considers a mixed phase consisting of a continuous fluid phase (non-mixed gas and liquid phases) and a dispersed phase of solid particles. To compute these flow fields, mass conservation equations and momentum conservation equations are calculated for the gas, liquid, and solid phases.

Assuming the material derivative for each phase is zero, i.e., $D\rho_k/Dt = 0$, the following volume conservation equation is derived from the mass conservation equation.

$$\frac{\partial f_s}{\partial t} + \nabla \cdot (f_s \mathbf{u}_s) = 0 \tag{1}$$

$$\frac{\partial f_l}{\partial t} + \nabla \cdot (f_l \mathbf{u}_l) = 0 \tag{2}$$

$$\frac{\partial f_g}{\partial t} + \nabla \cdot (f_g \mathbf{u}_g) = 0 \tag{3}$$

Here, t is time, $\mathbf{u}$ is the velocity vector, and f is the volume fraction. The subscripts s, l, and g denote the solid phase, liquid phase, and gas phase, respectively. Assuming equal liquid and gas phase velocities within the computational cell yields the following continuity equation.

$$\nabla \cdot (f_s \mathbf{u}_s) + \nabla \cdot (f_c \mathbf{u}_c) = 0 \tag{4}$$

Here, the subscript c denotes the continuous phase, meaning $f_c = f_l + f_g$ and $\mathbf{u}_c = \mathbf{u}_l = \mathbf{u}_g$.

The momentum conservation equation for the continuous phase is derived from the Navier-Stokes equations.

$$\begin{aligned}&\frac{\partial f_c \rho_c \mathbf{u}_c}{\partial t} + \nabla \cdot (f_c \rho_c \mathbf{u}_c \mathbf{u}_c) \\ &= -f_c \nabla P_c + \nabla \cdot \left(f_c(\mu_c + \mu_t)(\nabla \mathbf{u}_c + \nabla \mathbf{u}_c^{\mathrm{T}})\right) + f_c \rho_c \mathbf{g} + \beta_c(\mathbf{u}_s - \mathbf{u}_c)\end{aligned} \tag{5}$$

Here, ρ is the density, μ is the viscosity, $\mathbf{g}$ is the gravitational acceleration vector, P is the pressure, μ_t is the turbulent viscosity, and β is the drag coefficient. The density and viscosity of the continuous phase are defined by $f_c\rho_c = f_l\rho_l + f_g\rho_g$ and $f_c\mu_c = f_l\mu_l + f_g\mu_g$.

The equation for momentum conservation concerning the dispersed phase is given by the following equation.[15]

$$\begin{aligned}&\frac{\partial f_s \rho_s \mathbf{u}_s}{\partial t} + \nabla \cdot (f_s \rho_s \mathbf{u}_s \mathbf{u}_s) \\ &= -f_s \nabla P_c - \nabla P_s + \nabla \cdot (\boldsymbol{\tau}_s) + f_s \rho_s \mathbf{g} - \beta_c(\mathbf{u}_s - \mathbf{u}_c)\end{aligned} \tag{6}$$

where P_s is the pressure generated by mutual interference between solid particles, and $\boldsymbol{\tau}_s$ is the stress tensor. The pressure P_s and stress tensor $\boldsymbol{\tau}_s$ can be decomposed into kinetic and enduring-contact components,[15] namely $P_s = P_s^K + P_s^E$, and $\boldsymbol{\tau}_s = \boldsymbol{\tau}_s^K + \boldsymbol{\tau}_s^E$. The superscripts K and E denote the kinetic and enduring-contact components, respectively. The motion of solid particles is influenced by the surrounding fluid through the pressure gradient term $f_s \nabla P_c$ and the drag term $\beta_c(\mathbf{u}_s - \mathbf{u}_c)$ on the right-hand side of Equation (6).

Based on kinetic theory, the transport equation for the fluctuating energy Θ_s of solid particles is given by the following equation.[20]

$$\frac{3}{2}\left[\frac{\partial f_s \rho_s \Theta_s}{\partial t} + \nabla \cdot (f_s \rho_s \mathbf{u}_s \Theta_s)\right] = 2\boldsymbol{\tau}_s^K : \mathbf{S}_s + \nabla(\kappa_s^K \nabla \Theta_s) - \gamma_s^K - 3\beta_c \Theta_s \tag{7}$$

where Θ_s is the fluctuating energy of the solid particle, κ_s^K is the conductivity, γ_s^K is the energy dissipation due to collisions, and $\mathbf{S}$ represents the strain rate tensor. As described in Section 2.2, Θ_s is used to calculate the kinetic pressure P_s^K and the kinetic shear stress $\boldsymbol{\tau}_s^K$.

The following section discusses the constitutive equations for β_c, μ_t, P_s^K, $\boldsymbol{\tau}_s^K$, P_s^E, $\boldsymbol{\tau}_s^E$, κ_s^K, and γ_s^K.

2.2 Constitutive equations

The drag coefficient β_c in equations (5) to (7) is decomposed into solid-liquid and gas-liquid components, i.e., $\beta_c = (f_l/f_c)\beta_l + (f_g/f_c)\beta_g$. Each drag coefficient is given by the following equation.[20]

$$\beta_k = \begin{cases} 150\dfrac{f_s^2 \mu_k}{f_c d_s^2} + 1.75\dfrac{\rho_k f_s |\mathbf{u}_c - \mathbf{u}_s|}{d_s}, & f_c < 0.8 \\ \dfrac{3}{4} C_{D,k} \dfrac{f_c f_s \rho_k |\mathbf{u}_c - \mathbf{u}_s|}{d_s} f_c^{-2.65}, & f_c \geq 0.8 \end{cases} \quad (k = l \text{ or } g) \tag{8}$$

Here, the coefficient C_D is calculated using the following equation.[21]

$$C_{D,k} = 0.4 + \frac{24}{\mathrm{Re}_{p,k}} + \frac{6}{1 + \sqrt{\mathrm{Re}_{p,k}}} \tag{9}$$

Here, $\mathrm{Re}_{p,k}$ is the particle Reynolds number, given by $\mathrm{Re}_{p,k} = \rho_k |\mathbf{u}_c - \mathbf{u}_s| d_s / \mu_k$, where d_s is the particle diameter.

Large eddy simulation (LES)[22] is used as the turbulence model for the continuous phase. The turbulent viscosity μ_t is calculated from the following equation.

$$\mu_t = \rho_c (C_s \Delta_{\mathrm{cell}}^{1/3})^2 \sqrt{\frac{1}{2} |\mathbf{S}_c| |\mathbf{S}_c|} \tag{10}$$

Here, the coefficient C_s is set to 0.18, and Δ_{cell} is the volume of the computational grid.

The pressure P_s^K and P_s^E and the stress tensor $\boldsymbol{\tau}_s^K$ and $\boldsymbol{\tau}_s^E$ in Equation (6) are given by the following expressions.[15]

$$P_s^K = \rho_s f_s \Theta_s [1 + 2(1+e) f_s g_0] \tag{11}$$

$$P_s^E = P_s^{ES} + P_s^{EF} \tag{12}$$

$$\begin{aligned}P_s^{ES} = {} & K f_s [\max(f_s - f_{s,\min}, 0)]^{\chi} \\ & \left\{1 + \sin\left[\max\left(\frac{f_s - f_{s,\min}}{f_{s,\max} - f_{s,\min}}, 0\right)\pi - \frac{\pi}{2}\right]\right\}\end{aligned} \tag{13}$$

$$P_s^{EF} = \max(P_s^D - P_s^K, 0) \tag{14}$$

$$P_s^D = \rho_s \Theta_s \left[9\left(\frac{(1-e)\lambda^K}{\mu^K}\right)\left(\frac{a' f_s f_{s0}}{f_{s0} - f_s}\right)^{2/\delta}\right] \tag{15}$$

$$\boldsymbol{\tau}_s^K = \left[f_s \left(\xi_s^K - \frac{2}{3}\mu_s^K \right) \nabla \cdot \mathbf{u}_s \right] \mathbf{I} + 2 f_s \mu_s^K \mathbf{S}_s \tag{16}$$

$$\boldsymbol{\tau}_s^E = 2 P_s^E \eta^S \frac{1 - \exp(-n\|\mathbf{S}_s\|)}{2\|\mathbf{S}_s\|} \mathbf{S}_s \tag{17}$$

Here, $\mathbf{I}$ is the unit tensor, $\|\mathbf{S}\| = \sqrt{\mathbf{S}:\mathbf{S}/2}$ is the second invariant of tensor $\mathbf{S}$, g_0 is the radial distribution function, e is the rebound coefficient, $f_{s,\min}$ is the random loose packing fraction, $f_{s,\max}$ is the maximum solid fraction, and $\eta^S = \tan\theta^S$ is the friction coefficient, and θ^S is the internal static friction angle. As described later, the viscosity μ_s^K and the bulk viscosity ξ_s^K are given by kinetic theory. The coefficients K, χ, a', δ, n, and f_{s0} are model parameters. Lee et al.[15] investigated the influence of parameters and showed that their effects are smaller compared to the effect of θ^S. In this model, similar to their work, we used $K = 10^8$, $\chi = 1.5$, $a = 0.28$, $\delta = 0.58$, $n = 10^5$, and $f_{s0} = 0.6$. The elastic modulus e is given by the following equation.[23]

$$e = e_0 - 2.85\,\mathrm{St}^{-1/2} \tag{18}$$

Here, e_0 is the dry particle coefficient of restitution, and $\mathrm{St} = \rho_s d_s \Theta_s / 18\mu_c$ is the Stokes number. The radial distribution function g_0 is calculated from the following equation.[15]

$$g_0 = \frac{1 - 7/16}{(1 - f_s/f_{s,\max})^2} \tag{19}$$

In this model, the viscosity μ_s^K, bulk viscosity ξ_s^K, conductivity κ_s^K, and energy dissipation rate γ_s^K in kinetic theory are given by the following equations.[20]

$$\mu_s^K = \frac{4\rho_s d_s f_s g_0 (1+e)\Theta_s^{1/2}}{5\pi^{1/2}} \tag{20}$$

$$\xi_s^K = \frac{4\rho_s d_s f_s g_0 (1+e)\Theta_s^{1/2}}{3\pi^{1/2}} \tag{21}$$

$$\kappa_s^K = \frac{2\rho_s d_s f_s g_0 (1+e)\Theta_s^{1/2}}{\pi^{1/2}} \tag{22}$$

$$\gamma_s^K = 3(1-e^2) f_s^2 \rho_s g_0 \Theta_s \left(\frac{4\Theta_s^{1/2}}{d_s \pi^{1/2}} - \nabla \cdot \mathbf{u}_s \right) \tag{23}$$

3. Numerical Analysis Methods

Several studies have derived the volume-of-fluid equations from the mass conservation equation.[24, 25] This model uses Equation (2), the volume-of-liquid equation, to calculate the gas-liquid free surface. In the VOF method, the advection volume is calculated using techniques for capturing the free surface position, such as SLIC,[26] the donor-acceptor method,[6] and CICSAM.[27] **Figure 1** schematically shows the gas, liquid, and solid phases within a computational cell as assumed in this model. The position of the free surface is determined not by the volume of the liquid itself, but by the volume of the region where the liquid occupies the continuous phase. Since the volume fraction α within the latter cell is given by $\alpha = f_l/f_c$, Equation (2) can be rewritten as follows.

$$\frac{\partial f_l}{\partial t} + \nabla \cdot (\alpha f_c \mathbf{u}_c) = 0 \tag{24}$$

Therefore, the interface capture method must be applied to α in the convection term of Equation (24). This means decomposing the advection volume of the liquid into the advection volume of the continuous phase and the liquid fraction within the continuous phase.

Each conservation equation was discretized using the finite volume method. First-order upwind differences were applied to the convection terms in Equations (1), (5)–(7). For the convection term in Equation (24), the CICSAM scheme was applied to α, and first-order upwind differences were applied to f_c. Second-order central differences were applied to the diffusion terms in Equations (5)–(7).

Table 1 lists the parameters and material properties used in the numerical calculations of Chapter 4. In this study, similar to the work of Lee et al.[15], a random loose packing fraction $f_{s,\min} = 0.57$ and a maximum solid fraction $f_{s,\max} = 0.63$ were used. Furthermore, the coefficient of restitution, friction coefficient, density, viscosity, and particle size were set as shown in Table 1 according to each scenario.

4. Numerical Analysis Results

4.1 Granular collapse of heavy particles in water

Shademani et al.[18] reported on granular collapse in water through experiments and numerical calculations using the DEM-VOF method. This section compares numerical calculation results using this model with their findings.

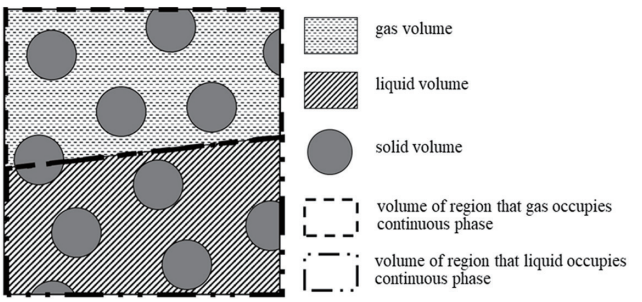

Fig. 1 Schematic of the gas, liquid, and solid phases in a computational cell assumed in the proposed model

Table 1 Parameters and physical properties used for numerical simulations

Section	Gas-liquid-solid phase	$f_{s,\min}$ [-]	$f_{s,\min}$ [-]	e_0 [m²/N]	η^S [-]	ρ [kg/m³]	μ [kg/ms]	d_s [mm]
4.1	(gas) air (liquid) water (solid) glass beads	0.57	0.63	0.9	0.4	$\rho_g = 1$ $\rho_l = 1\,000$ $\rho_s = 2\,500$	$\mu_g = 10^{-5}$ $\mu_l = 10^{-3}$	0.8
4.2	(gas) air (liquid) fresh water (FW) or salt water (SW) (solid) polypropylene beads	0.57	0.63	0.9	0.47	$\rho_g = 1$ $\rho_l = \begin{cases} 998\ (\mathrm{FW}) \\ 1\,180\ (\mathrm{SW}) \end{cases}$ $\rho_s = 910$	$\mu_g = 10^{-5}$ $\mu_l = 10^{-3}$	3.2
4.3	(gas) air (liquid) water (solid) various density particles	0.57	0.63	0.9	0.3	$\rho_g = 1$ $\rho_l = 1\,000$ $\rho_s = 200$–800	$\mu_g = 10^{-5}$ $\mu_l = 10^{-3}$	2.0

Figure 2 schematically shows the numerical calculation setup. As shown in Fig. 2, a two-dimensional numerical calculation of granular collapse in water was performed. The friction coefficient, density, viscosity coefficient, and particle size were set as shown in Table 1.[18] **Table 2** shows the conditions for the two cases, Case S1 and Case S2. The initial length l_0 and height h_0 were set to (l_0, h_0) = (0.0975, 0.049) for Case S1 and (l_0, h_0) = (0.0575, 0.084) for Case S2. The initial solid volume fraction in the powder was set to 0.57. Furthermore, the gate holding the powder accumulation was removed vertically at the same speed of 1 m/s as in the experiment. At the boundary surfaces, no-slip conditions were applied for gas, liquid, and solid flows, and the normal gradient of energy was set to zero.

Figure 3 compares snapshots from this model with those reported by Shademani et al.[18]. The results are shown at each nondimensional time $T = t/\tau_0$, where τ_0 is the characteristic time defined as $\tau_0 = \sqrt{h_0/|\mathbf{g}|}$. The black lines in the figure represent contour lines for α = 0.5. To compare with Shademani et al.'s results, a color function ϕ = 0−1 was defined for the solid phase, and the following transport equation was computed:

$$\frac{\partial f_s \phi}{\partial t} + \nabla \cdot (f_s \phi \mathbf{u}_s) = 0 \qquad (25)$$

Figure 3 shows that the numerical calculations using this model exhibit good agreement with DEM-VOF numerical calculations and experiments. The final sediment shape is determined by whether the initial aspect ratio h_0/l_0 is above or below the critical value of 0.75.[28] As shown in Fig. 3, at T = 10.0, the granular body forms a trapezoidal deposit in Case S1 ($h_0/l_0 < 0.75$) and a triangular deposit in Case S2 ($h_0/l_0 > 0.75$), consistent with previous findings.

Figure 4 compares the collapse distance between this model and the DEM-VOF method. In this calculation, the collapse distance l was estimated as the distance from the left wall to the position where $f_s = 0.95\, f_{s,\min}$. The calculation results were normalized by $(l - l_0)/h_0$, where l_0 and h_0 are the initial granular body length and height, respectively. As shown in Fig. 4, the curves of the dimensionless collapse distance became nearly equal for Cases S1 and S2. Furthermore, the calculation results from this model and the DEM-VOF method agreed very well, confirming the validity of this model.

It is known that negative pressure develops within the initial granular body during granular collapse when the initial granular body is dense.[29] **Figure 5** shows the time evolution of fluid pressure at the bottom of the granular body for cases with an initial solid fraction of 0.57 (sparsely packed) and 0.61 (densely packed). In the sparsely packed case, the granular body contracts initially, causing the fluid phase to exhibit positive pressure. Conversely, in the densely packed case, the packed layer expands initially, causing the fluid phase to exhibit negative pressure. A similar phenomenon was observed in Rondon et al.'s[29] experiments on granular collapse in viscous fluids. This result further demonstrates that the present

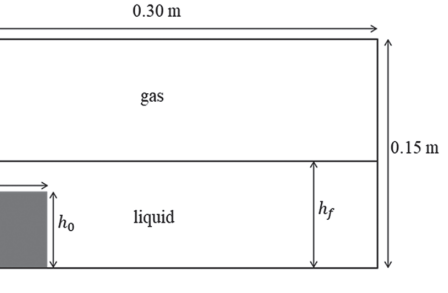

Fig. 2 Setup of numerical simulations for submerged granular collapse

Table 2 Conditions of numerical simulations for submerged granular collapse

	Column length, l_0	Column height, h_0	Water depth, h_f
Case S1	0.0975 m	0.049 m	0.07 m
Case S2	0.0575 m	0.084 m	0.10 m

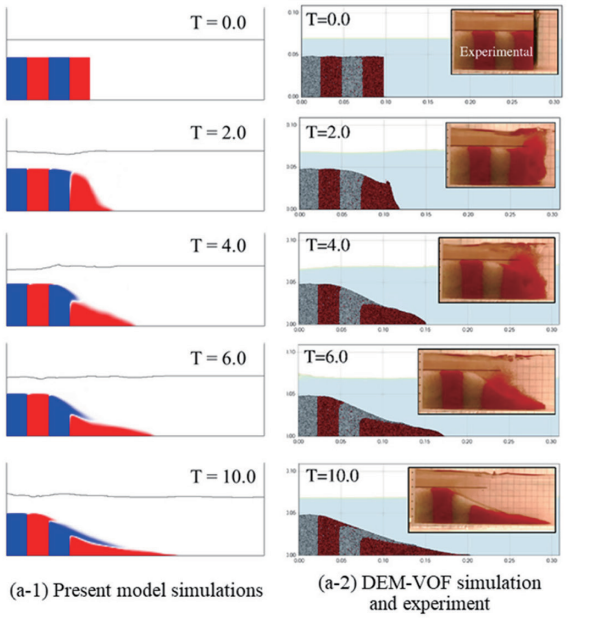

Fig. 3 Comparisons of the snap-shots between the proposed model simulations, the DEM-VOF simulations, and experiments by Shademani et al. (2021). Reproduced under the terms of the Creative Commons Attribution License (Shademani et al.[18]). Copyright 2021, MDPI.

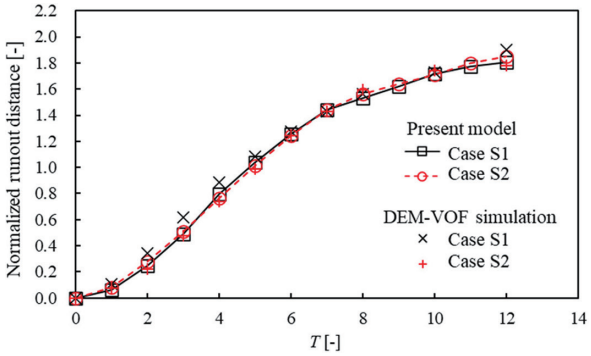

Fig. 4 Comparisons of the runout distance between the proposed model simulations and the DEM-VOF simulations by Shademani et al. (2021)

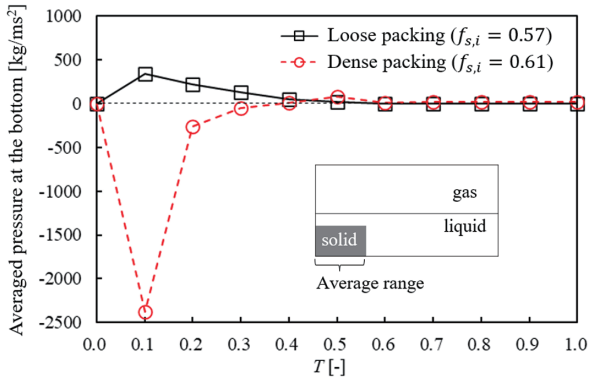

Fig. 5 Time evolution of averaged pressure in liquid phase at the onset of the granular collapse

model effectively reproduces the behavior of the solid-phase filling phase and the surrounding fluid associated with it.

4.2 Granular collapse of light particles on the water surface

Zheng et al.[19] conducted experiments on the flow of floated particles along a gas-liquid interface. Unlike the granular collapse of heavy particles described in Section 4.1, their experiments involved solid particles with a density lower than that of the liquid, causing the solid particles to float at the gas-liquid interface. This section compares numerical calculations using this model with their experimental results.

Figure 6 schematically shows the numerical calculation setup. As shown in Fig. 6, a three-dimensional numerical calculation of floated granular collapse was performed. The rebound coefficient e_0 was set to 0.9.[30] The friction coefficient η^s was set to 0.47, corresponding to a static internal friction angle $\theta^s \approx 25°$. The density and particle diameter were set as shown in Table 1.[19] Furthermore, the viscosities of gas and water were set to $\mu_g = 10^{-5}$ and $\mu_l = 10^{-3}$, respectively. **Table 3** shows the conditions for the two cases denoted as Case SW and Case FW. The liquid phase is saltwater in Case SW and freshwater in Case FW. The initial granular volume fraction was set to $f_{s0} = 0.57$. Since Reference 19) does not mention the gate opening speed, the gate was ignored in the numerical calculations. At the interface, a no-slip condition was applied for the gas, liquid, and solid flows, and the normal gradient of energy was set to zero.

Figure 7 shows the calculated solid particle distribution. The black lines in the figure represent contour lines for $\alpha = 0.5$. The figure shows that solid particles propagate along the gas-liquid interface over time. Figure 7(b) indicates that the shape of the propagation front is smooth in the early collapse stage but gradually becomes rougher in the final stage. This trend was also observed in Zheng et al.'s experiments, and the present calculation results reproduce the experimental results well.

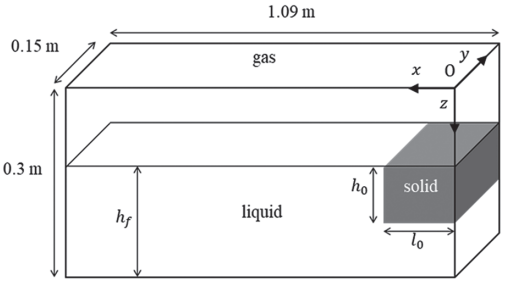

Fig. 6 Setup of numerical simulations for floating granular collapse

Table 3 Conditions of numerical simulations for floating granular collapse

	Liquid	Column length, l_0	Column height, h_0
Case SW	salt water	0.101 m	0.096 m
Case FW	fresh water	0.109 m	0.092 m

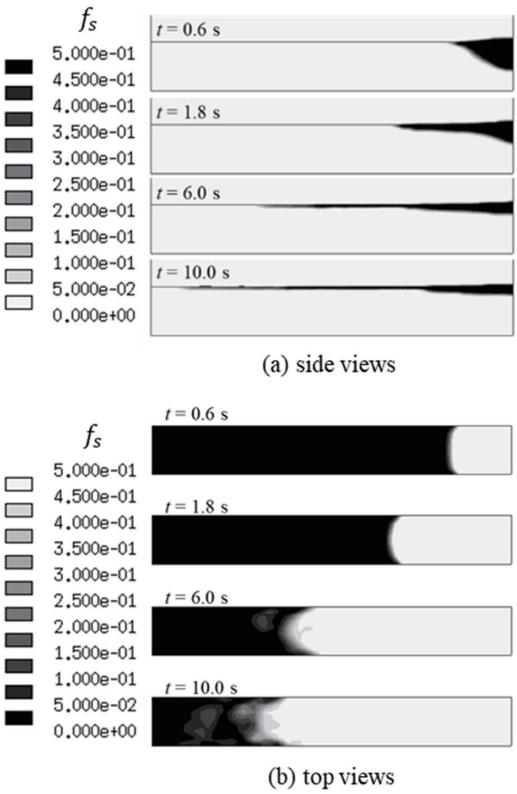

Fig. 7 Snap-shots of the proposed model simulations of Case SW

Zheng et al.[19] reported that the collapse distance l can be approximated by the following equation:

$$l = at^b \tag{26}$$

Figure 8 compares the collapse distance between this model and the experiment. Here, the experimental results are plotted using the reported values of a and b[19]. In the numerical calculation, the col-

lapse distance was calculated as the length from the right wall to the position where $f_s = 0.95\, f_{s,\min}$. As shown in Fig. 8, the numerical calculation results from this model show good agreement with the experimental results, although a slight discrepancy is observed in Case SW. The difference between Case SW and Case FW stems from the difference in liquid density ρ_l. It can be seen that the propagation velocity is faster in Case SW, where the density difference between the solid and liquid phases is greater, than in Case FW.

4.3 Floatation and oscillation of light particles on the water surface

When the density of a solid is less than that of a liquid, solid particles float at the gas-liquid interface. **Figure 9** shows a bed of light solid particles floating at the gas-liquid interface. Due to the balance of forces, the ratio of the immersion length h to the total length H is $h/H = \rho_s/\rho_l$. Furthermore, when the packed bed shifts vertically from its equilibrium position, it exhibits simple harmonic motion with a period $T_h = 2\pi\sqrt{\rho_s H/\rho_l|\mathbf{g}|}$ if there is no fluid resistance. This section confirms that numerical calculations using this model satisfy these relationships: $h/H = \rho_s/\rho_l$ and $T_h = 2\pi\sqrt{\rho_s/H/\rho_l|\mathbf{g}|}$.

Figure 10 schematically shows the numerical calculation setup. As shown in Fig. 10, a two-dimensional numerical calculation was performed where a solid packing layer freely falls toward the gas-liquid interface. Solid particles initially positioned above the gas-liquid interface fall toward the interface under gravity, land on the surface, pass through the equilibrium position, and then oscillate near the interface. The solid density was varied from 200 to 800, while the liquid density was fixed at 1 000. The coefficient of restitution $e_0 = 0.9$ and the friction coefficient $\eta^S = 0.3$ were used. The initial solid volume fraction $f_{s0} = 0.5$ was assumed. At the interface, slip conditions were applied to the gas, liquid, and solid flows, and the normal gradient of energy was set to zero.

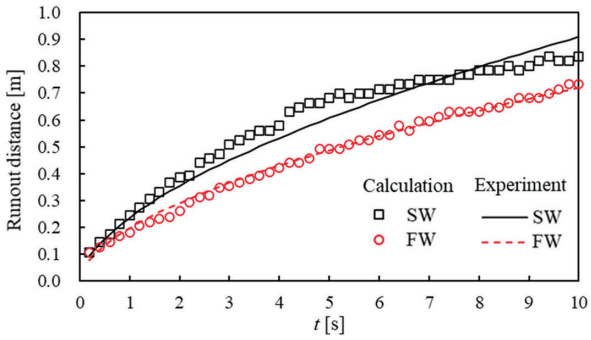

Fig. 8 Comparisons of the runout distance between simulations and experiments[19)]

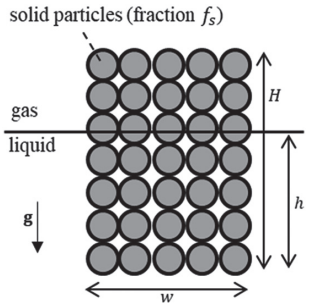

Fig. 9 Illustration of floatation of blocked solid particles on a gas-liquid surface

The y-coordinate of the solid particle's center of gravity was calculated using the following equation.

$$y_c = \frac{\sum f_{s,i} y_i}{\sum f_{s,i}} \tag{27}$$

Here, the subscript i denotes the cell index, and only cells satisfying $f_s > 0.95\, f_{s,\min}$ are included in the summation. Next, the time-averaged center position $\overline{y_c}$ of the solid particles was calculated. The time-averaging window was set to $t = 3$–6 seconds. **Figure 11** shows the time evolution of the deviation $y_c - \overline{y_c}$ for $\rho_s/\rho_l = 0.2$, 0.4, 0.6, and 0.8. The figure reveals distinct oscillatory behavior in the solid phase center of mass, with both the amplitude and period of oscillation increasing as the density ratio ρ_s/ρ_l increased.

To confirm that the calculation results satisfy the relationship $h/H = \rho_s/\rho_l$, the time-averaged immersion depth $\overline{h}$ and the time-averaged filling layer height $\overline{H}$ were calculated. The filling layer height was defined as the height in the region where $f_s > 0.95\, f_{s,\min}$. Furthermore, the position of the gas-liquid interface y_i was defined as the position corresponding to $\alpha = 0.5$. The time-averaged immersion depth $\overline{h}$ is calculated as $\overline{h} = \overline{H}/2 + (\overline{y_c} - \overline{y_i})$, where $\overline{y_i}$ is the time-averaged interface position. Furthermore, to confirm that the calculation results satisfy the relationship $T_h = 2\pi\sqrt{\rho_s H/\rho_l|\mathbf{g}|}$, the correct period $T_e = 2\pi\sqrt{\rho_s \overline{H}/\rho_l|\mathbf{g}|}$ was evaluated using the time-averaged height $\overline{H}$. Furthermore, the period T_c of solid vibration was estimated from the

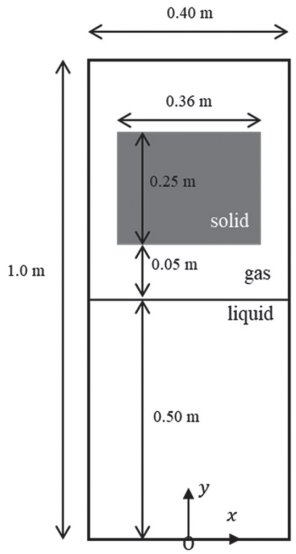

Fig. 10 Setup of numerical simulations for floatation and oscillation on a gas-liquid surface

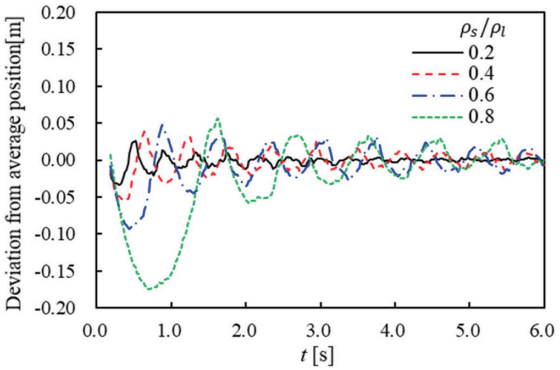

Fig. 11 Time evolution of the center position of solid phase

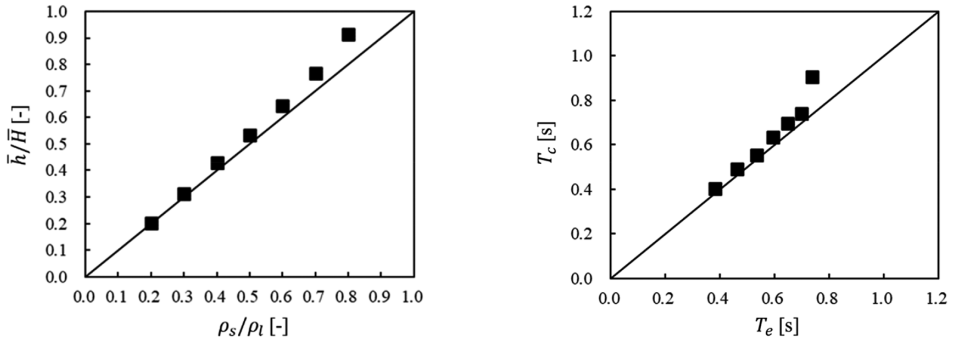

(a) Immersion length (b) Oscillation period

Fig. 12 Comparisons of the simulation results with the theoretical relationships for the immersion length and oscillation period

time-varying curve of $y_c - \bar{y}_c$ (Fig. 11). **Figure 12** (a) shows a comparison of the calculated values $\bar{h}/\bar{H}$ and the density ratio ρ_s/ρ_l, while Fig. 12 (b) shows a comparison of T_c and T_e. The figures indicate that the calculated results generally agree with theoretical predictions, demonstrating that this model can accurately calculate the floatation and oscillation behavior of solid particles. When the density ratio is large, the calculated values are higher than the theoretical predictions. This is because the packed bed overshoots below the gas-liquid interface, deviating from the situation assumed in Fig. 9.

In conclusion, this model enabled quantitative calculation of the floatation and oscillation of solid particles due to gravity and buoyancy. This model is also applicable to situations where the motion of a free interface and solid particles coexist. The reasonable liquid phase behavior, where the liquid phase occupies the particle voids neither excessively nor insufficiently while particle motion occurs, is achieved through the coupling method with the VOF method described in Chapter 3. This coupling method plays a crucial role in this model.

5. Conclusion

This study developed a numerical computational model for solid-gas-liquid three-phase flow based on a continuum description. The flow field is computed for the dispersed phase consisting of solid particles and the continuous phase comprising immiscible gas and liquid phases. For the solid phase, a particle model considering both kinetic and static effects was applied to simultaneously compute the flow of dispersed and sedimented solid particles. For the gas and liquid phases, the VOF method was used to compute the free surface. Coupling the VOF method with the particle model enabled numerical calculations of solid-gas-liquid three-phase flow where the free surface and solid particle flow coexist. To validate this model, numerical calculations were performed for the following three cases and compared with experiments and theoretical solutions, confirming the model's sufficient applicability to solid-gas-liquid three-phase flow.

The first case involved granular collapse of heavy solid particles. In this case, there was no interaction between the solid phase and the gas-liquid interface; instead, flow of the particulate material occurred within a liquid pool. Comparison of DEM-VOF calculations with literature experiments showed good agreement in the behavior of granular collapse and the time evolution of the collapse distance.

The second case involved the floated granular collapse of light solid particles. Here, the solid particles flowed along the gas-liquid interface. The results of this calculation showed a similar trend to the experimental results from previous studies, with good agreement in the temporal evolution of the collapse distance between the two.

The third case involved a system where a bed of light particles floats and oscillates at the gas-liquid interface. Here, solid particles oscillate near the gas-liquid interface due to gravity and buoyancy. The immersion length and oscillation period of the bed obtained from the calculations satisfied the theoretical relationship for simple harmonic motion.

References

1) Lei, S., Zhang, J., Zhao, X., He, K.: Numerical simulation of molten steel flow and inclusions motion behavior in the solidification processes for continuous casting slab. ISIJ Int. 54, 94–102 (2014)
2) Raziyeh, S., Ataallah, S.G.: CFD simulation of an industrial hydrocyclone with Eulerian-Eulerian approach: A case study. Int. J. Min. Sci. Technol. 24, 643–648 (2014)
3) Xie, L., Luo, Z.H.: Modeling and simulation of the influences of particle-particle interactions on dense solid-liquid suspensions in stirred vessels. Chem. Eng. Sci. 176, 439–453 (2018)
4) Peng, Z., Galvin, K., Doroodchi, E.: Influence of inclined plates on flow characteristics of a liquid-solid fluidized bed: A CFD-DEM study. Powder Technol. 343, 170–184 (2019)
5) Wu, S., Kou, M., Xu, J., Guo, X., Du, K., Shen, W., Sun, J.: DEM simulation of particle size segregation behavior during charging into and discharging from a Paul-Wurth type hopper. Chem. Eng. Sci. 99, 314–323 (2013)
6) Hirt, C.W., Nichols, B.D.: Volume of fluid (VOF) for the dynamics of free boundaries. J. Comput. Phys. 39, 201–225 (1981)
7) Sussman, M., Smereka, P., Osher, S.: A level set approach for computing solutions to incompressible two-phase flow. J. Comput. Phys. 114, 146–159 (1994)
8) Sun, X., Sakai, M.: Three-dimensional simulation of gas-solid-liquid flows using the DEM-VOF method. Chem. Eng. Sci. 134, 531–548 (2015)
9) Ding, J., Gidaspow, D.: A bubbling fluidization model using kinetic theory of granular flow. AIChE J. 36, 523–538 (1990)
10) Peirano, E., Delloume, V., Johnsson, F., Leckner, B., Simonin, O.: Numerical simulation of the fluid dynamics of a freely bubbling fluidized bed: influence of the air supply system. Powder Technol. 122, 69–82 (2002)
11) Lettieri, P., Felice, R.D., Pacciani, R., Owoyemi, O.: CFD modelling of liquid fluidized beds in slugging mode. Powder Technol. 167, 94–103 (2006)
12) Ouriemi, M., Aussillous, P., Guazzelli, E.: Sediment dynamics. Part 1. Bed-load transport by laminar shearing flows. J. Fluid Mech. 636, 295–319 (2009)
13) Lagrée, P.-Y., Staron, L., Popinet, S.: The granular column collapse as a continuum: validity of a two-dimensional Navier-Stokes model with a μ(I)-rheology. J. Fluid Mech. 686, 378–408 (2011)
14) GDR MiDi: On dense granular flows. Eur. Phys. J. E 14, 341–365 (2004)
15) Lee, C.H., Huang, Z., Chiew, Y.M.: A three-dimensional continuum model incorporating static and kinetic effects for granular flows with ap-

plications to collapse of a two-dimensional granular column. Phys. Fluids. 27, 113303 (2015)
16) Hsu, T.J., Jenkins, J.T., Liu, P.L.-F.: On two-phase sediment transport: sheet flow of massive particles. Proc. R. Soc. A 460, 2223–2250 (2004)
17) Peyneau, P.-E., Roux, J.-N.: Frictionless bead packs have macroscopic friction, but no dilatancy. Phys. Rev. E 78, 011307 (2008)
18) Shademani, M., Blais, B., Shakibaeinia, A.: CFD-DEM modeling of dense sub-aerial and submerged granular collapses. Water. 13, 2969 (2021)
19) Zheng, Z., Huppert, H.E., Vriend, N.M., Neufeld, J.A., Linden, P.F.: Flow of buoyant granular materials along a free surface. J. Fluid Mech. 848, 312–339 (2018)
20) Gidaspow, D., Bezburuah, R., Ding, J.: Hydrodynamics of circulating fluidized beds: kinetic theory approach. In: Fluidization VII, Proceedings of the 7th Engineering Foundation Conference on Fluidization, 75–82 (1992)
21) White, F.M.: Viscous Fluid Flow. McGraw-Hill, New York, 1974, p.209
22) Deardorff, J.W.: A numerical study of three-dimensional turbulent channel flow at large Reynolds numbers. J. Fluid Mech. 41, 453–480 (1970)
23) Armanini, A., Larcher, M., Fraccarollo, L.: Intermittency of rheological regimes in uniform liquid-granular flows. Phys. Rev. E 79, 051306 (2009)
24) Wörner, M., Sabisch, W., Grötzbach, G., Cacuci, D.G.: Volume-averaged conservation equations for volume-of-fluid interface tracking. In: Proceedings of the 4th International Conference on Multiphase Flow, New Orleans, Louisiana, USA (2001)
25) Yamamoto, T., Takatani, K.: Pressure-based unified solver for gas-liquid two-phase flows where compressible and incompressible flows coexist. Int. J. Numer. Methods Fluids. 88, 277–295 (2018)
26) Noh, W.F., Woodward, P.: SLIC (simple line interface calculation). In: Proceedings of the 5th International Conference on Numerical Methods in Fluid Dynamics, June 28–July 2, 1976 Twente University, Enschede. Springer, 330–340 (1976)
27) Ubbink, O., Issa, R.I.: A method for capturing sharp fluid interfaces on arbitrary meshes. J. Comput. Phys. 153, 26–50 (1999)
28) Bougouin, A., Lacaze, L.: Granular collapse in a fluid: Different flow regimes for an initially dense-packing. Phys. Rev. Fluids. 3, 064305 (2018)
29) Rondon, L., Pouliquen, O., Aussillous, P.: Granular collapse in a fluid: Role of the initial volume fraction. Phys. Fluids. 23, 073301 (2011)
30) Kaneko, Y., Shiojima, T., Horio, M.: DEM simulation of fluidized beds for gas-phase olefin polymerization. Chem. Eng. Sci. 54, 5809–5821 (1999)

Kengo KIHARA
Researcher
Mathematical Science & Technology Research Lab.
Advanced Technology Research Laboratories
20-1 Shintomi, Futtsu City, Chiba Pref. 293-8511

Nobuhiro OKADA
Ph. D., General Manager, Head of Dept.
Mathematical Science & Technology Research Lab.
Advanced Technology Research Laboratories